MATERIALS SCIENCE

Thin-film composite vapor-gap membrane for pressure-driven distillation

Li Zhang[1,2], Tianxiang Yang[1,2], Zhenyi Zhao[1,2], Zhi Wang[1,2], Shihong Lin[3,4]*, Song Zhao[1,2]*

Pressure-driven distillation (PD), as an emerging technology, holds tremendous potential for producing freshwater from nontraditional water sources. In this process, a sufficient hydraulic pressure is applied to drive water evaporation and vapor transport across a vapor-gap membrane. The development of the PD process critically depends on the availability of robust and large-area superhydrophobic membranes. Here, we propose an ultraselective superhydrophobic thin-film composite (TFC) vapor-gap membrane with confined transport channels toward the PD process, which can be manufactured scale-up through a facile swelling–assisted deposition strategy. The TFC-PD membrane demonstrates separation capabilities, achieving near-complete rejections of nonvolatile solutes, including salts, boron, and urea. Featured by a vapor-gap superhydrophobic layer, the TFC-PD membrane exhibits superior chlorine and scaling resistance and maintains stable performance over time without being oxidized or scaling. This work offers notable advancements in the microstructural design of PD membranes and the development of scalable robust TFC membranes for the PD process.

INTRODUCTION

Global and regional water scarcity has necessitated the augmentation of the water supply from nontraditional sources, including wastewater, seawater, and brackish water (*1*–*3*). Reverse osmosis (RO) is now the most widely used membrane separation technology for producing potable water from a variety of nontraditional sources (*4*–*6*). Despite its extensive applications, the efficiency of the RO process is often limited by the inherent trade-off between water permeability and solute selectivity (*7*–*9*). Moreover, RO membranes usually struggle to effectively remove neutral solutes with low molecular weights, such as boron, urea, and disinfection byproducts, requiring additional posttreatment to achieve high-quality product water (*10*). In addition to these challenges, polyamide-based RO membranes are susceptible to active chlorine due to *N*-chlorination at amide groups or direct ring chlorination, and thus, a series of costly pretreatment steps, e.g., disinfection and dechlorination, is required for the control of biofouling and oxidation (*11, 12*). Therefore, there is an urgent need to develop an innovative, robust membrane that can simplify the pretreatment steps and exhibit chemical inertness toward pollutants and oxidants, thereby providing technical support for the sustainable production of high-quality freshwater.

Pressure-driven distillation (PD) has been identified as a potential alternative to the current RO process due to its near-perfect selectivity, similar energy efficiency, and oxidation resistance (*13*–*15*). In the PD process, the evaporation of water molecules and the subsequent vapor transport process in a vapor-gap layer are driven by applying a sufficient hydraulic pressure to the feed solution, thereby creating a partial vapor pressure gradient across the membrane (*16, 17*). The hydraulically driven PD process is fundamentally distinct from temperature-driven membrane distillation, which suffers from inevitable thermal loss and severe temperature polarization (*18*–*20*). In general, the vapor-gap hydrophobic layer of the PD membrane plays a pivotal role in separation, which serves as a channel for vapor diffusion and an antiwetting barrier, enabling the near-complete rejection of nonvolatile solutes.

The feasibility of desalination via the PD process has been validated through both theoretical and experimental investigations. Theoretical analyses have demonstrated the practical viability of PD technology and provided guiding principles for the design of efficient PD membranes (*14, 16*). The reported PD membranes achieved water fluxes comparable to those of RO membranes and efficient removal of more than 99% of nonvolatile solutes, as well as resistance to chlorine and oxidants (*13, 15*). However, the development of PD membranes is still insufficient, particularly concerning the absence of scalable fabrication strategies applicable to polymeric membranes. Consequently, it is imperative to focus on designing a high-performance polymeric membrane tailored for the PD process to enhance its practical applications.

In this work, we propose a robust and ultraselective superhydrophobic membrane with confined transport channels toward the PD process. The fabricated thin-film composite PD (TFC-PD) membrane consists of a fluorosilica superhydrophobic layer and a polydimethylsiloxane-incorporated cucurbituril molecule (PDMS@CB) vapor-permeable layer. The elastic siloxane backbone of the PDMS network allows for rearrangement of the chains, thereby promoting stable deposition of the fluorosilica layer (*21, 22*). The water vapor transport mechanism in the TFC-PD membrane is analyzed via molecular dynamic simulations. The TFC-PD membrane exhibits near-complete rejections of nonvolatile solutes, including salts, boron, and urea. In addition, the TFC-PD membrane demonstrates desalination performance in resisting gypsum scaling and chlorinated oxidation. The findings of this work underscore an effective strategy for the large-scale production of robust TFC membranes for the PD process, thus providing a notable impetus for future advancements in ultraselective PD membranes.

RESULTS

Design and assembly of the TFC-PD membrane

During the PD process, the hydraulic pressure applied on the feed side induces curvature at the gas-liquid interface, leading to the

[1]School of Chemical Engineering and Technology, Tianjin University, Tianjin 300072, P. R. China. [2]Tianjin Key Laboratory of Membrane Science and Desalination Technology, State Key Laboratory of Chemical Engineering, Tianjin University, Tianjin 300072, P. R. China. [3]Department of Civil and Environmental Engineering, Vanderbilt University, Nashville, TN 37235-1831, USA. [4]Department of Chemical and Bimolecular Engineering, Vanderbilt University, Nashville, TN 37235-1831, USA.
*Corresponding author. Email: shihong.lin@vanderbilt.edu (S.L.); songzhao@tju.edu.cn (S.Z.)

formation of a convex meniscus against the vapor gap (Fig. 1A). The transmembrane partial vapor pressure difference serves as the primary driving force for water evaporation at the convex meniscus, vapor transport within the gap, and subsequent condensation on the distillate side (table S1). The hydrophobicity and pore radius of the vapor-gap membrane are critical factors in the implementation of the PD process. On the basis of the Young-Laplace equation, it is necessary to decrease the membrane pore radius and enhance hydrophobicity to maintain a nonwetting state under high hydraulic pressure, thereby preserving the functionality of the vapor-gap layer (Fig. 1B). In addition, under a given hydraulic pressure, an increase in membrane thickness can notably improve the resistance to pore wetting (Fig. 1C). Thermodynamic analysis indicates that the thickness of the TFC-PD membrane exceeds the minimum threshold required to prevent pore wetting, as calculated on the basis of both applied hydraulic pressure and pore radius determined from scanning electron microscopy (SEM) images.

Consequently, we designed a three-layer composite TFC-PD membrane comprising a fluorosilica superhydrophobic layer, a PDMS@CB vapor-permeable layer, and a polymeric substrate (Fig. 1D). The hydrophilic substrate not only provides essential mechanical strength to withstand high water pressures but also effectively facilitates liquid permeation from the distillate side (*23, 24*). The PDMS@CB layer forms an interconnected network by integrating the PDMS matrix with macrocyclic CB having an inner cavity of 3.9 Å (*25*), thereby functioning as confined transport channels for vapor-phase diffusion. The fluorosilica superhydrophobic layer adheres firmly to the PDMS@CB layer, creating a nanometer-thick vapor-gap layer that promotes rapid vapor diffusion and minimizes temperature polarization (*26, 27*).

The physicochemical properties of CB molecules were confirmed through electrostatic potential (ESP) calculation using the Gaussian 16 package. The ESP map reveals a negative value of −45.7 kcal mol^{-1} at carbonyl oxygen (blue), verifying its strong polarity capable of disrupting hydrogen bonds inside water-polar clusters (Fig. 1E). Moreover, the inner cavity with a positive ESP value indicates the absence of functional groups or electron pairs pointing toward the inside, providing a rationale for its pronounced hydrophobicity (*28*). In addition, the permanent porosity of CB molecules was verified through an N_2 adsorption-desorption experiment, with calculated theoretical Brunauer-Emmett-Teller surface area, total pore volume, and pore size distribution being 87 $m^2 g^{-1}$, 0.045 $cm^3 g^{-1}$, and 3.7 Å, respectively (figs. S1 and S2), which were highly consistent with the simulated structure (fig. S3), and the literature *(29, 30)*.

The fluorosilica superhydrophobic layer was constructed via a facile swelling–assisted deposition strategy, achieving a water contact angle (WCA) of 161°. The pronounced superhydrophobicity of this layer could be attributed to the abundant —CF_3 and —CF_2— bonds derived from the grafting of perfluorinated chains onto the silica surface, which was verified through analyses of the ultraviolet-visible (UV-vis) spectrum, ^{19}F solid-state nuclear magnetic resonance (NMR) spectrum, and x-ray diffractometer pattern (figs. S4 to S6). Owing to its amorphous structural flexibility and thermal stability, the fluorosilica layer is capable of dissipating external stress

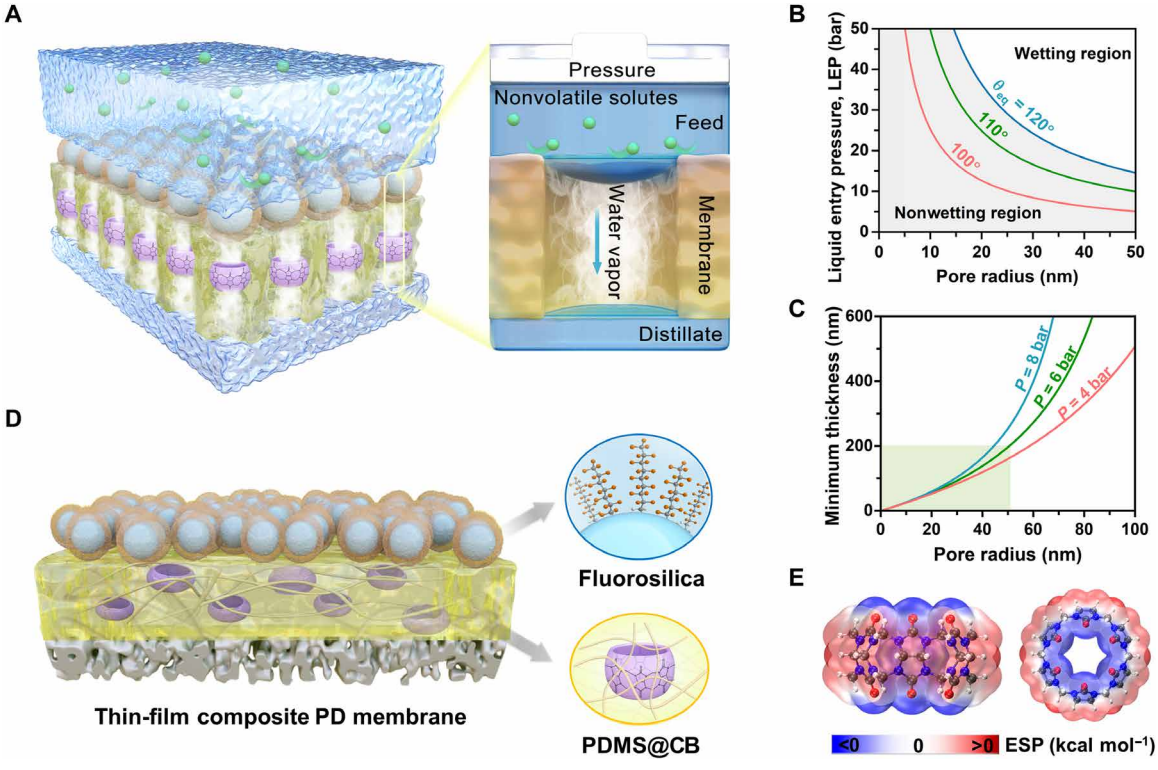

Fig. 1. Design of vapor-gap membranes for vapor transport based on pressure-driven distillation. (**A**) Schematic diagram of pressure-driven water vapor transport through a vapor gap within the TFC-PD membrane. (**B**) Liquid entry pressure (LEP) as a function of pore radius with three different intrinsic water contact angles (WCAs). (**C**) Modeled minimum possible thickness as a function of pore radius under various applied pressures (assuming θ_{eq} = 120°). (**D**) Schematic diagram of the three-layer composite structure of the TFC-PD membrane. (**E**) Electrostatic potential (ESP) map of CB molecule (side view and top view).

by the stretching of Si—O—Si bonds while maintaining exceptional thermal stability under PD process conditions (*31*).

Structural characterization of the TFC-PD membrane

The deposition of fluorosilica on the TFC-PD membrane was confirmed through the analysis of the Fourier transform infrared (FTIR) spectrum (Fig. 2A and fig. S7). The FTIR spectrum of the TFC-PD membrane revealed the emergence of new peaks at 1010, 788, and 1250 cm^{-1}, corresponding to Si—O—Si and C—F groups, respectively (*32*). In addition, new characteristic peaks at 1257 and 1727 cm^{-1} appeared in the FTIR spectrum of the PDMS@CB layer, corresponding to the C—Si groups in PDMS and C═O groups in CB, indicating the successful incorporation of CB into the PDMS network (*33, 34*).

Subsequently, elemental compositions on the TFC-PD membrane surface were confirmed through x-ray photoelectron spectroscopy (XPS). Five primary peaks were identified, including C 1s at ~293 eV, O 1s at ~534 eV, F 1s at ~690 eV, Si 2s at ~155 eV, and Si 2p at ~105 eV (*35*), accounting for 24.2, 24.1, 37.2, and 14.5%, respectively (Fig. 2B), suggesting the successful deposition of fluorosilica layer onto the membrane surface. The high-resolution deconvoluted C 1s XPS spectrum revealed the presence of —CF_3 bonds at ~294.9 eV, —CF_2— bonds at ~292.6 eV, —C—F bonds at ~290 eV, —C—O— bonds at ~286.6 eV, and —C—C—/—C—Si— bonds at ~284.6 eV (Fig. 2C) (*36*–*38*). The —CF_2— bonds, accounting for 42.8%, endow the TFC-PD membrane surface with ultralow surface energy and exceptional superhydrophobicity. Relevant characteristic peaks were also observed in the deconvoluted F 1s and Si 2p spectra (figs. S8 and S9). Moreover, energy-dispersive x-ray spectroscopy (EDS) images showed a uniform distribution of silicon, oxygen, fluorine, and carbon, indicating a homogeneous surface composition of the TFC-PD membrane (fig. S10).

Furthermore, the spherically shaped fluorosilica nanoparticles were observed to be densely stacked and firmly attached to the membrane surface, with an average surface roughness of 428.7 nm (Fig. 2D and fig. S11). The voids between these nanoparticles facilitate air trapping, thereby preserving superhydrophobicity and promoting a stable Cassie-Baxter state (*39, 40*). The uniform distribution of fluorosilica nanoparticles over the surface of the TFC-PD membrane was also evidenced by bright orange regions with high Raman intensity, derived from the even distribution of Si—O—Si bonds in the Raman image of the laser confocal microscopy (Fig. 2, E and F). Moreover, the composite vapor-gap layer was observed to be composed of an ~50-nm-thick fluorosilica superhydrophobic layer and an ~150-nm-thick PDMS@CB layer (fig. S11). The thin-layer structure notably reduces the transfer resistance and mitigates the detrimental effect of reverse transmembrane temperature difference on the driving force (*41, 42*).

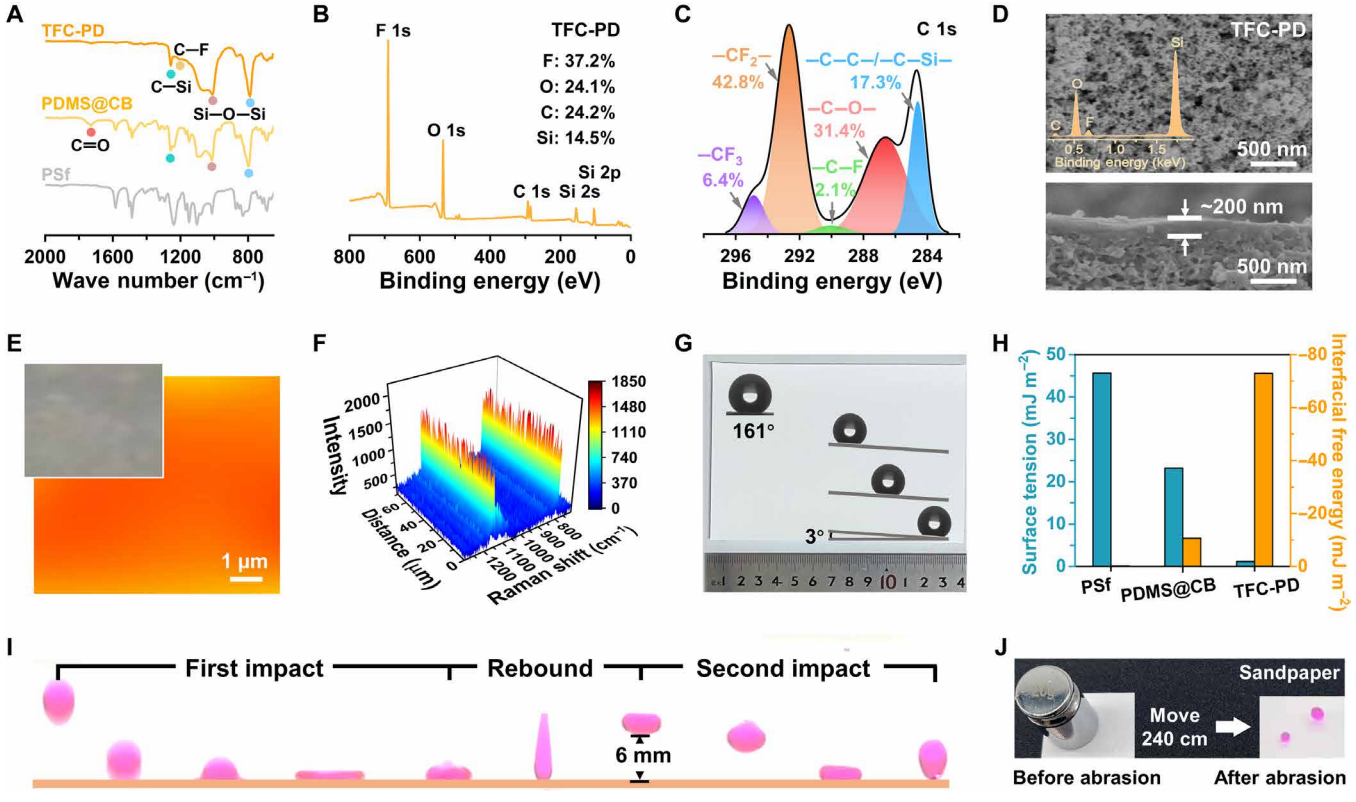

Fig. 2. Characterization of the chemical composition, morphology, superhydrophobicity, and abrasion resistance of the TFC-PD membrane. (**A**) FTIR spectra of the PSf substrate, PDMS@CB membrane, and TFC-PD membrane. (**B**) Full x-ray photoelectron spectroscopy (XPS) survey spectrum and surface element composition of the TFC-PD membrane. (**C**) High-resolution deconvoluted C 1s XPS spectrum of the TFC-PD membrane. (**D**) Surface and cross-sectional SEM images of the TFC-PD membrane. (**E**) Surface optical microscopy image and Raman mapping of the TFC-PD membrane. (**F**) Raman spectra at different positions of the TFC-PD membrane. (**G**) Digital photograph, WCA, and sliding angle of the TFC-PD membrane. (**H**) Surface tension and interfacial free energy of the PSf substrate, PDMS@CB membrane, and TFC-PD membrane. (**I**) Digital photographs of the TFC-PD membrane with the impact/bounce of a water droplet on the surface. (**J**) Sandpaper abrasion test of the TFC-PD membrane.

The large-area fabrication of the TFC-PD membrane measuring 9 cm by 14 cm was readily achieved, with size determined by the laboratory fabrication frame, indicating considerable potential for scalable manufacturing. The surface of the TFC-PD membrane demonstrated superhydrophobic characteristics with a WCA of 161°, a sliding angle below 3°, a surface tension of 1.2 mJ m^{-2}, and an interfacial free energy of −73 mJ m^{-2} (Fig. 2, G and H), which endowed the membrane with exceptional wetting resistance even under high hydraulic pressure (*43*). The ultrahigh WCA of the TFC-PD membrane is primarily attributed to the deposition of the fluorosilica layer, in contrast to the hydrophilic polysulfone (PSf) substrate having a WCA of 75° and hydrophobic PDMS@CB layer having a WCA of 114° (fig. S12).

The TFC-PD membrane also demonstrated excellent dynamic superhydrophobicity and water-repellent properties, which were validated through the determination of WCA and sliding angle, alongside observations of water-jet repellency (figs. S13 to S15 and movies S1 and S2). Furthermore, water droplets with a volume of 10 μl could rebound up to six times on the surface, reaching maximum bounce heights of up to 6 mm (Fig. 2I) (*44*). The number of consecutive droplet rebounds serves as a substantial indicator of dynamic wetting resistance of the surface, likely contributing to enhanced foulant resistance and self-cleaning properties. Notably, the TFC-PD membrane demonstrated abrasion resistance, as evaluated by a standard sandpaper abrasion test, which could withstand an abrasion distance of 240 cm without compromising its superhydrophobicity (Fig. 2J).

The surface of the TFC-PD membrane exhibited a strong negative charge, with a zeta potential of −41.5 mV measured at pH 7.3 and an isoelectric point of approximately 3.2 (fig. S16). The negatively charged surface of the membrane primarily stems from the electronegativity of the C—F moiety (*45*), alongside the preferential adsorption of hydroxyl ions onto the liquid-hydrophobic interface (*46*), which is anticipated to enhance the scaling resistance property of the membranes through electrostatic repulsion. The structural homogeneity and vapor permeation property of the TFC-PD membrane were assessed by measuring the gas permeance under a pressure of 1 bar. The TFC-PD membrane exhibited extremely low N_2 permeance, indicating a continuous, dense, and defect-free layer. In addition, the water vapor permeance of the TFC-PD membrane was measured at 294 gas permeance unit (GPU) (fig. S17), which verified the construction of an effective water vapor transport channel in the vapor-gap layer.

Desalination performance of the TFC-PD membrane

The desalination performance of the TFC-PD membrane was assessed using a dead-end stirred cell immersed in a constant temperature water bath. The separation capability of the TFC-PD membrane was evaluated with aqueous solutions of lithium chloride (LiCl), potassium chloride (KCl), cesium chloride (CsCl), and sodium chloride (NaCl) having different ionic diameters ranging from 0.12 to 0.34 nm. The TFC-PD membrane achieved near-complete rejections exceeding 99% for all the tested salts (Fig. 3A), indicating that the underlying separation mechanism predominantly relied on gas-liquid phase transition rather than size exclusion. Specifically, the exceptional salt rejections of the TFC-PD membrane can be primarily attributed to the superhydrophobic layer formed by fluorosilica deposition. Conversely, the PDMS@CB membrane without the superhydrophobic layer exhibited lower salt rejections of nearly 80%, which can be ascribed to the adverse effect of liquid permeation. Furthermore, the PDMS@CB membrane demonstrated a higher rejection for salts with larger ionic diameters, suggesting that its separation process is primarily governed by size exclusion.

Subsequently, when the NaCl salinity was increased to 3000 parts per million (ppm; 50 mM), a gradual decline in the flux of the TFC-PD membrane was observed, whereas the NaCl rejection consistently remained above 99% (fig. S18). As mentioned above, hydraulic pressure applied to the feed side generates a net transmembrane vapor pressure difference that serves as the driving force facilitating water evaporation and vapor transport. Nevertheless, high salt concentrations tend to suppress the vapor pressure on the feed side, thereby restricting the net vapor pressure and leading to reduced flux.

Molecular dynamic simulation of vapor transport behavior

Molecular dynamic simulations validated the vapor transport channels provided by CB molecules within the TFC-PD membrane. Compared with the fluorosilica/PDMS membrane devoid of CB molecules, the incorporation of CB molecules introduced vapor-phase–confined transport channels, thereby enhancing the flux of the TFC-PD membrane (Fig. 3B). The CB molecules have a portal diameter of 3.9 Å, comparable to that of water molecules (2.6 Å). The similarity in molecular size facilitates the rearrangement of intermolecular hydrogen bonds in water, enabling rapid transport through the confined channels. In addition, the inner cavity of each CB molecule, featuring a high degree of symmetry and hydrophobicity, can notably reduce the frictional collision between vapor molecules and channel walls, contributing to nearly frictionless surface slippage (*25*). Furthermore, hydrophilic carbonyl groups at the edge of CB molecules can effectively disrupt hydrogen bonds inside water-polar clusters in the bulk system, facilitating the capture and subsequent entry of water molecules into the confined transport channels. On the basis of the quantum tunneling fluid effect, wettability plays a crucial role in transport behavior. The presence of ordered molecular chains within hydrophobic confinement notably enhances the transport of water molecules (*47*).

Molecular dynamic simulations further elucidated the transport behavior of vapor molecules within the PDMS and PDMS@CB networks on a microscopic scale (Fig. 3C). The total energy of vapor molecule transport through the confined transport channels was calculated to rationalize the transport mechanism of vapor molecules. The simulation results indicated that water vapor molecules at the entrance of the channel exhibited the highest total energy of −1040.2 kcal mol^{-1}. As water vapor molecules entered the channel, the total energy decreased gradually until it reached a saddle point of −1042.5 kcal mol^{-1}, indicating their complete entry into the inner cavity of CB molecules. This observation aligns with theoretical predictions that suggest spontaneous filling in the hydrophobic inner cavity. The free volumes of the PDMS and PDMS@CB networks were calculated on the basis of the constructed molecular structures (Fig. 3, D and G). The fractional free volume (FFV; gray and blue regions) for the PDMS@CB network was found to be 25.9%, surpassing that of the PDMS network of 22.1%. The increase in the FFV can primarily be attributed to the incorporated CB molecules with a large cavity volume into the interconnected PDMS network.

Simulations were conducted to examine the transport trajectories of water vapor molecules within the PDMS and PDMS@CB networks at 0, 0.4, 1, and 2 ns (Fig. 3, E and H). Water vapor molecules initially reached equilibrium on the feed, followed by a rapid transfer from the feed side to the distillate side through the PDMS@CB network within 2 ns. In contrast, the transport of water vapor

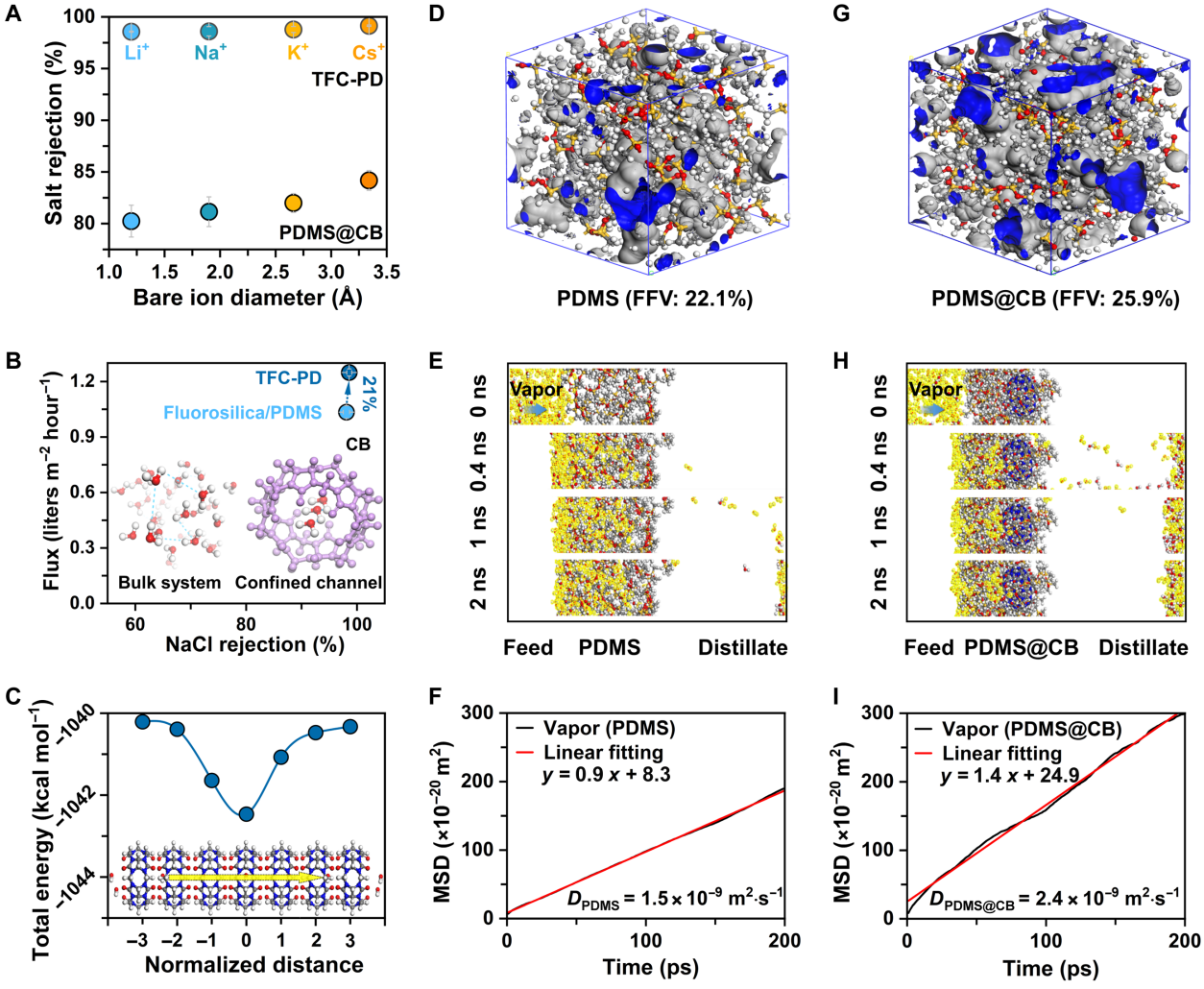

Fig. 3. Desalination performance of the TFC-PD membrane and molecular dynamic simulations. (**A**) Rejections of salts with bare ion diameters ranging from 0.12 to 0.34 nm at a concentration of 1000 parts per million (ppm) by the TFC-PD and PDMS@CB membranes, under an operating pressure of 6 bar and a temperature of 90°C. (**B**) Comparison of NaCl rejection and flux of the TFC-PD membrane and fluorosilica/PDMS membrane. (**C**) The total energy of concerted water vapor molecule transport through CB molecules. (**D** and **G**) Amorphous cells of the PDMS and PDMS@CB networks constructed by molecular dynamic simulation. (**E** and **H**) Transport trajectories of water vapor within both the PDMS and PDMS@CB networks during molecular dynamic simulations at 0, 0.4, 1, and 2 ns. (**F** and **I**) The corresponding calculated mean square displacement (MSD) values of water vapor molecules within the simulation time in the PDMS and PDMS@CB networks.

molecules in the PDMS network occurred at a slower rate, suggesting a limited quantity of water vapor. The diffusion coefficients for water vapor molecules in both networks were calculated using linear fitting of mean square displacement (MSD) curves based on the Einstein relationship (*48*). The diffusion coefficient of the PDMS@CB network (2.35×10^{-9} m^2 s^{-1}) was approximately 1.6 times higher than that of the PDMS network (1.48×10^{-9} m^2 s^{-1}), which was consistent with the experimental data and theoretical analyses presented above (Fig. 3, F and I).

Neutrally charged solute rejections of the TFC-PD membrane

The separation performance of the TFC-PD membrane demonstrated the characteristics of pressure-driven water vapor flow with a linear increase in flux, as the applied pressure increased from 1 to 6 bar (Fig. 4A). In addition, under an applied pressure of 6 bar, the temperature increased within the PD system led to an enhancement in vapor flux from 0.6 liters m^{-2} $hour^{-1}$ at 60°C to 1.3 liters m^{-2} $hour^{-1}$ at 90°C. The enhanced flux is primarily attributed to the rise in equilibrium vapor pressure with increasing temperature, governed by the Antoine equation. In addition, the TFC-PD membrane exhibited stable operation at high temperatures up to 90°C, effectively addressing the challenges associated with the RO desalination process under high-temperature conditions.

Another key advantage of the PD process lies in its near-complete rejection of small neutrally charged solutes, such as boron and urea, thereby avoiding the traditional trade-off between permeability and selectivity. The TFC-PD membrane achieved an impressive boron rejection of 98.2% and a urea rejection of 97% (Fig. 4B). The superior rejections for small neutrally charged solutes are attributed to the dual functionality of the gas-liquid interface, which not only

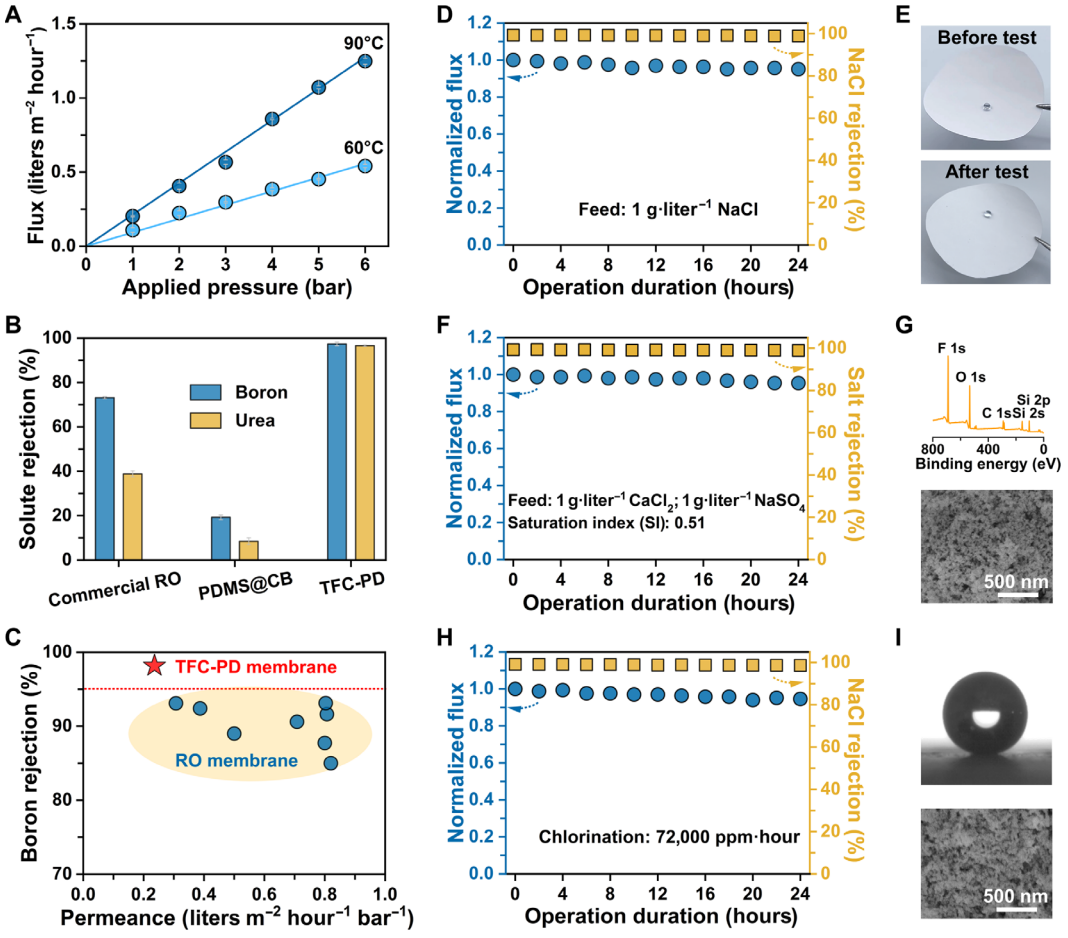

Fig. 4. Rejections for neutrally charged solutes, performance stability, scaling resistance, and oxidation resistance of the TFC-PD membrane. (**A**) Measured fluxes as a function of applied hydraulic pressures of the TFC-PD membrane at temperatures of 60° and 90°C, with hydraulic pressures ranging from 1 to 6 bar. (**B**) Boron and urea rejections of PDMS@CB and TFC-PD membranes evaluated at 6 bar and 90°C or commercial RO membrane evaluated at 10 bar and 25°C. (**C**) A comparative analysis of boron rejection and flux of the TFC-PD membrane with the state-of-the-art RO membranes reported in the literature. (**D**) Performance stability of the TFC-PD membrane evaluated using a feed solution of 1000-ppm NaCl over 24 hours of continuous operation at 6 bar and 90°C. (**E**) Digital photographs of the TFC-PD membrane after the desalination test. (**F**) Scaling resistance of the TFC-PD membrane evaluated using a model gypsum solution, comprising 1000-ppm $CaCl_2$ and 1000-ppm Na_2SO_4 with a saturation index (SI) of 0.51. (**G**) Full XPS spectrum and surface SEM image of the TFC-PD membrane after the mineral scaling experiment. (**H**) Chlorine resistance of the TFC-PD membrane evaluated by exposure to a 2000-ppm NaClO solution for 36 hours. (**I**) WCA and surface SEM image of the TFC-PD membrane after chlorine exposure.

enhances water evaporation but also serves as a barrier against the penetration of liquids into the vapor-gap layer. In contrast, the PDMS@CB membrane, with a weaker hydrophobicity, exhibited boron and urea rejection rates of only 19.2 and 8.5%, respectively. Furthermore, commercial polyamide RO membranes also showed limited performance, with a boron rejection of only 73.7% and a urea rejection of only 40.2%, primarily due to the ineffective electrostatic repulsion caused by the neutral charge of boric acid (H_3BO_3) and urea molecules, as well as the limited size exclusion effects (Fig. 4B). Consequently, the TFC-PD membrane exhibited comparable water permeance and superior rejection for small neutrally charged solutes in comparison to the current state-of-the-art RO membranes (Fig. 4C) (*49*–*56*).

Scaling and oxidation resistance of the TFC-PD membrane

The TFC-PD membrane demonstrated stable desalination performance, with fluctuations below 5% throughout a 24-hour continuous operation (Fig. 4D). After the desalination test, the superhydrophobicity of the membrane was retained, further confirming its excellent stability and considerable potential for practical applications (Fig. 4E and fig. S19).

The mineral scaling resistance of the TFC-PD membrane was evaluated using a model gypsum solution containing 1000-ppm calcium chloride ($CaCl_2$) and 1000-ppm sodium sulfate (Na_2SO_4). The membrane maintained the flux and salt rejection throughout a 24-hour continuous operation (Fig. 4F). In addition, the surface morphology of the membrane was well preserved after the operation, exhibiting no characteristic indicators of gypsum crystal formation (Fig. 4G and fig. S20). The scaling resistance of the TFC-PD membrane can be primarily attributed to its superhydrophobic surface, which effectively prevents interfacial crystallization by notably reducing contact area and adhesion.

The TFC-PD membrane exhibited exceptional resistance to chlorination, with negligible changes in its separation performance after exposure to a 2000-ppm sodium hypochlorite (NaClO) solution for 36 hours (Fig. 4H). No notable alterations in the WCA or surface morphology were observed after the 24-hour continuous

operation (Fig. 4I). The chlorine resistance of the TFC-PD membrane is primarily due to the inherent insensitivity of the fluorosilica layer to chlorine attack (*57, 58*).

DISCUSSION

This work achieves a major milestone by developing an ultraselective superhydrophobic TFC vapor-gap membrane that features confined vapor transport channels to achieve separation performance in the PD process. Relying on the gas-liquid phase change, the TFC-PD membrane demonstrated near-complete rejections of the tested nonvolatile solutes, including salts, boron, and urea. The vapor-gap layer serves as an impermeable separation barrier, endowing the membrane with scaling resistance and stable desalination performance even after chlorine exposure. Furthermore, molecular dynamic simulations were used to further elucidate the transport mechanism of water vapor within the confined channel. This work provides an effective route for fabricating robust and large-area superhydrophobic membranes that achieve near-complete rejection of nonvolatile solutes, representing a notable advancement in the development and application of polymeric membranes with ultrahigh desalination capability.

MATERIALS AND METHODS

Materials and chemicals

Tetraethoxysilane (TEOS; 98%) was purchased from Aladdin Reagent. *n*-Heptane [analytical reagent (AR)], KCl (98%), and anhydrous NaCl (AR) were obtained from Jiangtian Chemical Technology. Boric acid (AR) was obtained from Kermel Chemical Reagent. Anhydrous $CaCl_2$ (AR) and anhydrous Na_2SO_4 (AR) were obtained from Kermel Chemical Reagent. Urea (AR), LiCl (99%), CsCl (99%), 1*H*,1*H*,2*H*,2*H*-perfluorodecyltriethoxysilane (PFDTES; 98%), and anhydrous magnesium sulfate ($MgSO_4$; 98%) were supplied by Heowns Biochem Technologies. Cucurbit[6]uril (CB) was obtained from D&B Biological Science and Technology. Silica (particle size of 15 nm, 99.5%) was provided by Zancheng Technology. NaClO (4.0% available chlorine) was obtained from Macklin Biochemical Technology. PDMS was purchased from Shin-Etsu Chemical. Dibutyltin dilaurate (DBD) was supplied by Yuanli Chemical. The PSf substrate (molecular weight cutoff of 60 kDa) was provided by Vontron Membrane Technology. Commercial polyamide RO membranes (SW30) were obtained from Dow Chemical. Deionized water with a conductivity of less than 15 μS cm^{-1} was produced using an ultrapure water purification system.

Preparation of the PDMS@CB suspension

The PDMS@CB suspension was prepared by the following procedures. PDMS (1.5 g), TEOS (1.2 g), and DBD (1.2 g) were dissolved in *n*-heptane (98.7 g), which was continuously stirred for 90 min at 60°C. The CB (30 mg) was subsequently dispersed into the above solution and stirred for 30 min. The suspension was placed in an artificial climate chamber at 30°C and 40% relative humidity for preservation.

Preparation of the fluorosilica suspension

Hydrophilic silica nanoparticles (69 mg) were dispersed into *n*-heptane (40 ml) and then stirred at ambient temperature for 10 min. Subsequently, TEOS (0.4 g) and PFDTES (1.0 g) were added. After reacting at ambient temperature for 2 hours under magnetic stirring, a fluorosilica suspension was obtained.

Fabrication of the TFC-PD membrane

The TFC-PD membrane consists of a fluorosilica superhydrophobic layer, a PDMS@CB vapor-permeable layer, and a polymeric substrate. First, the PDMS@CB suspension was poured onto the top surface of the PSf substrate for 10 min and evenly spread on the membrane surface at 60°C. Subsequently, the residual PDMS solution was removed, and the membrane was transferred to a drying process for an additional 10 min in an artificial climate chamber to obtain the PDMS@CB membrane. Afterward, the surface of the PDMS@CB membrane was further exposed to fluorosilica suspension and allowed for even dispersion for 10 min under thermal treatment at 60°C. Subsequently, the residual suspension was removed completely, and the membrane was rinsed several times with *n*-heptane. Last, the TFC-PD membrane was dried and stored in an artificial climate chamber at 30°C and 40% relative humidity. The fabrication of the fluorosilica/PDMS membrane was conducted with the same procedures described above, except for the use of the PDMS@CB suspension.

Fluorosilica powder characterization

The chemical structure of the fluorosilica powder was analyzed by the ^{19}F solid-state NMR spectroscopy (JNM-ECZ600R, JEOL). The crystalline structure of silica and fluorosilica was investigated through x-ray diffraction (D8 Focus, Bruker). The chemical composition of the fluorosilica powder was analyzed via FTIR spectroscopy (FTS-6000, Bio-Rad). The chemical structure of fluorosilica powder was determined by a UV-vis spectrophotometer (TU-1810).

Membrane characterization

The surface and cross-sectional morphologies and EDS mappings of the membranes were observed by SEM (S-4800, Hitachi). The surface roughness of the membranes was evaluated by atomic force microscopy (Dimension Icon, Bruker) with a scanning range of 5 μm × 5 μm. The surface chemical composition of the membranes was determined by FTIR spectroscopy (FTS-6000, Bio-Rad), XPS (ESCALAB 250Xi, Thermo Fisher Scientific), and microconfocal Raman spectrometer (inVia, Renishaw Trading). The hydrophilicity of the membrane surface was assessed through contact angle measurements conducted using a DataPhysics goniometer (OCA15EC). In addition, the zeta potential of the membrane surface was determined using a solid surface zeta potential analyzer (SurPASS, Anton Paar).

Separation performance tests

The separation performance of the membranes was evaluated using a laboratory-scale dead-end setup (fig. S21). The membranes were sealed within a stainless steel dead-end filtration cell with an effective surface area of ~14.5 cm^2. Subsequently, the membranes were subjected to precompaction at an applied pressure of 6 bar. Both the feed and distillate solutions were maintained at a temperature of 90.0° ± 0.5°C for a minimum duration of 30 min to ensure stable conditions, with the exception of the commercial polyamide RO membrane, which was operated at an applied pressure of 10 bar and a temperature of 25°C. The rejections of the membranes were evaluated using aqueous solutions of inorganic salts at a concentration of 1000 ppm and neutrally charged solutes (5-ppm boron and 500-ppm urea). The flux (*J*; in liters per square meter per hour)

and permeance (P; in liters per square meter per hour per bar) were calculated using Eqs. 1 to 3

$$J = \frac{M}{A \cdot \Delta t} \quad (1)$$

$$P = \frac{J}{\Delta P - \Delta \pi} \quad (2)$$

$$\Delta \pi = \Delta C_S \cdot R \cdot T \quad (3)$$

where M (in kilograms) is the weight of the distillate solution collected within the appointed time Δt (in hours), A (per square meter) represents the effective membrane area in the practical measurement, and $\Delta P - \Delta \pi$ (in bar) represents the driving force of the transmembrane transport. $\Delta \pi$ represents the osmotic pressure difference between the feed and distillate solutions, T (in kelvin) represents the absolute temperature, ΔC_S (in molar) refers to the ion concentration difference, and R (8.314 J mol^{-1} K^{-1}) is the gas constant.

The salt rejection was evaluated by a series of single salt solutions, while the salt concentrations in the distillate and feed solutions were measured by a conductivity meter (DDSJ-308A, China). The salt rejection (R, %) was defined as Eq. 4

$$R = \left(1 - \frac{C_d}{C_f}\right) \times 100 \quad (4)$$

where C_d and C_f (in milligrams per liter) are in accordance with the salt concentrations in the distillate and feed solutions, respectively. The concentrations of boron in the distillate and feed solutions were measured by an inductively coupled plasma optical emission spectrometry (5110, Agilent). The concentrations of urea were determined by a UV-vis spectrophotometer (TU-1810, China).

Molecular dynamic simulation

Molecular dynamic simulations were conducted using the Materials Studio software with a COMPASS force field. The PDMS and PDMS@CB networks were constructed, and the transport trajectories and diffusion coefficients of water vapor molecules in both networks were investigated by molecular dynamic simulations.

Initially, two three-dimensional periodic cells (2.5 nm by 2.5 nm by 2.5 nm) were established with periodic boundary conditions applied in all three dimensions. For the PDMS network, 10 PDMS chains (with a degree of polymerization of 10) were randomly incorporated into the cell. In the case of the PDMS@CB network, 10 PDMS chains (with a degree of polymerization of 10) and 3 CB molecules were randomly blended into the cell. Subsequently, the crosslinking processes were conducted at a temperature of 298.15 K. The networks were optimized using the Forcite module to achieve a thermodynamic equilibrium state characterized by minimum energy and then continuously relaxed to optimize their configurations within an isothermal-isobaric [constant particle number, pressure, and temperature (NPT)] ensemble.

A simulation box was established to obtain theoretical insights into the transport of water vapor molecules within both networks. The networks were positioned at the center of the simulation box, dividing the box into feed and distillate sections. In each section, 800 water vapor molecules were introduced to the feed side, and a constant force was applied to each molecule to achieve the desired pressures. Following this, a 10-ns NVT (constant particle number, volume, and temperature) simulation was implemented using a time step of 1 fs. The Andersen thermostat was used to maintain a consistent temperature of 363.15 K throughout the process. Notably, the silicon atoms in both networks were fixed during these simulations. On the basis of the Einstein relationship, the water vapor diffusion coefficients of both networks can be estimated by linear fitting and calculating the slopes of the MSD curves.

Supplementary Materials

The PDF file includes:

Supplementary Text
Figs. S1 to S23
Tables S1 to S6
Legends for movies S1 to S5
References

Other Supplementary Material for this manuscript includes the following:

Movies S1 to S5

REFERENCES AND NOTES

1. M. Elimelech, W. A. Phillip, The future of seawater desalination: Energy, technology, and the environment. *Science* **333**, 712–717 (2011).
2. J. R. Werber, C. O. Osuji, M. Elimelech, Materials for next-generation desalination and water purification membranes. *Nat. Rev. Mater.* **1**, 16018 (2016).
3. C. L. Ritt, M. Liu, T. A. Pham, R. Epsztein, H. J. Kulik, M. Elimelech, Machine learning reveals key ion selectivity mechanisms in polymeric membranes with subnanometer pores. *Sci. Adv.* **8**, eabl5771 (2022).
4. D. L. Gin, R. D. Noble, Designing the next generation of chemical separation membranes. *Science* **332**, 674–676 (2011).
5. M. Heiranian, H. Fan, L. Wang, X. Lu, M. Elimelech, Mechanisms and models for water transport in reverse osmosis membranes: History, critical assessment, and recent developments. *Chem. Soc. Rev.* **52**, 8455–8480 (2023).
6. K. Zuo, W. Wang, A. Deshmukh, S. Jia, H. Guo, R. Xin, M. Elimelech, P. M. Ajayan, J. Lou, Q. Li, Multifunctional nanocoated membranes for high-rate electrothermal desalination of hypersaline waters. *Nat. Nanotechnol.* **15**, 1025–1032 (2020).
7. L. Wang, M. S. Boutilier, P. R. Kidambi, D. Jang, N. G. Hadjiconstantinou, R. Karnik, Fundamental transport mechanisms, fabrication and potential applications of nanoporous atomically thin membranes. *Nat. Nanotechnol.* **12**, 509–522 (2017).
8. H. Qiu, M. Xue, C. Shen, Z. Zhang, W. Guo, Graphynes for water desalination and gas separation. *Adv. Mater.* **31**, e1803772 (2019).
9. H. B. Park, J. Kamcev, L. M. Robeson, M. Elimelech, B. D. Freeman, Maximizing the right stuff: The trade-off between membrane permeability and selectivity. *Science* **356**, eaab0530 (2017).
10. M. Di Vincenzo, A. Tiraferri, V.-E. Musteata, S. Chisca, R. Sougrat, L.-B. Huang, S. P. Nunes, M. Barboiu, Biomimetic artificial water channel membranes for enhanced desalination. *Nat. Nanotechnol.* **16**, 190–196 (2021).
11. Y. Yao, P. Zhang, F. Sun, W. Zhang, M. Li, G. Sha, L. Teng, X. Wang, M. Huo, R. M. DuChanois, T. Cao, C. Boo, X. Zhang, M. Elimelech, More resilient polyester membranes for high-performance reverse osmosis desalination. *Science* **384**, 333–338 (2024).
12. K. L. Cho, A. J. Hill, F. Caruso, S. E. Kentish, Chlorine resistant glutaraldehyde crosslinked polyelectrolyte multilayer membranes for desalination. *Adv. Mater.* **27**, 2791–2796 (2015).
13. D. T. Nguyen, S. Lee, K. P. Lopez, J. Lee, A. P. Straub, Pressure-driven distillation using air-trapping membranes for fast and selective water purification. *Sci. Adv.* **9**, eadg6638 (2023).
14. W. Liu, R. Wang, A. P. Straub, S. Lin, Membrane design criteria and practical viability of pressure-driven distillation. *Environ. Sci. Technol.* **57**, 2129–2137 (2023).
15. D. T. Nguyen, K. P. Lopez, S. Lee, J. Lee, M. T. Hernandez, A. P. Straub, Water desalination via pressure-driven distillation with chlorine-resistant and large-area polymeric membranes. *Environ. Sci. Technol. Lett.* **10**, 711–717 (2023).
16. K. P. Lopez, R. Wang, E. A. Hjelvik, S. Lin, A. P. Straub, Toward a universal framework for evaluating transport resistances and driving forces in membrane-based desalination processes. *Sci. Adv.* **9**, eade0413 (2023).
17. J. Lee, R. Karnik, Desalination of water by vapor-phase transport through hydrophobic nanopores. *J. Appl. Phys.* **108**, 044315 (2010).
18. A. Politano, P. Argurio, G. Di Profio, V. Sanna, A. Cupolillo, S. Chakraborty, H. A. Arafat, E. Curcio, Photothermal membrane distillation for seawater desalination. *Adv. Mater.* **29**, 1603504 (2017).

19. D. Hou, T. Li, X. Chen, S. He, J. Dai, S. A. Mofid, D. Hou, A. Iddya, D. Jassby, R. Yang, L. Hu, Z. J. Ren, Hydrophobic nanostructured wood membrane for thermally efficient distillation. *Sci. Adv.* **5**, eaaw3203 (2019).
20. B. Zhang, P. W. Wong, J. Guo, Y. Zhou, Y. Wang, J. Sun, M. Jiang, Z. Wang, A. K. An, Transforming $Ti_3C_2T_x$ MXene's intrinsic hydrophilicity into superhydrophobicity for efficient photothermal membrane desalination. *Nat. Commun.* **13**, 3315 (2022).
21. J. E. Mark, Some interesting things about polysiloxanes. *Acc. Chem. Res.* **37**, 946–953 (2004).
22. D. Qi, K. Zhang, G. Tian, B. Jiang, Y. Huang, Stretchable electronics based on PDMS substrates. *Adv. Mater.* **33**, 2003155 (2021).
23. C. Z. Liang, M. Askari, L. T. Choong, T.-S. Chung, Ultra-strong polymeric hollow fiber membranes for saline dewatering and desalination. *Nat. Commun.* **12**, 2338 (2021).
24. A. P. Straub, C. O. Osuji, T. Y. Cath, M. Elimelech, Selectivity and mass transfer limitations in pressure-retarded osmosis at high concentrations and increased operating pressures. *Environ. Sci. Technol.* **49**, 12551–12559 (2015).
25. K. I. Assaf, W. M. Nau, Cucurbiturils: From synthesis to high-affinity binding and catalysis. *Chem. Soc. Rev.* **44**, 394–418 (2015).
26. M. P. Wolf, G. B. Salieb-Beugelaar, P. Hunziker, PDMS with designer functionalities—Properties, modifications strategies, and applications. *Prog. Polym. Sci.* **83**, 97–134 (2018).
27. S. Song, D.-M. Drotlef, C. Majidi, M. Sitti, Controllable load sharing for soft adhesive interfaces on three-dimensional surfaces. *Proc. Natl. Acad. Sci. U.S.A.* **114**, E4344–E4353 (2017).
28. H. Nie, Z. Wei, X.-L. Ni, Y. Liu, Assembly and applications of macrocyclic-confinement-derived supramolecular organic luminescent emissions from cucurbiturils. *Chem. Rev.* **122**, 9032–9077 (2022).
29. S. Lim, H. Kim, N. Selvapalam, K.-J. Kim, S. J. Cho, G. Seo, K. Kim, Cucurbit[6]uril: Organic molecular porous material with permanent porosity, exceptional stability, and acetylene sorption properties. *Angew. Chem. Int. Ed. Engl.* **47**, 3352–3355 (2008).
30. Y. Zhang, G. Zhang, X. Xiao, Q. Li, Z. Tao, Cucurbit[*n*]uril-based supramolecular separation materials. *Coord. Chem. Rev.* **514**, 215889 (2024).
31. F. Wang, L. Dou, J. Dai, Y. Li, L. Huang, Y. Si, J. Yu, B. Ding, In situ synthesis of biomimetic silica nanofibrous aerogels with temperature-invariant superelasticity over one million compressions. *Angew. Chem. Int. Ed. Engl.* **59**, 8285–8292 (2020).
32. Y. Si, L. Wang, X. Wang, N. Tang, J. Yu, B. Ding, Ultrahigh-water-content, superelastic, and shape-memory nanofiber-assembled hydrogels exhibiting pressure-responsive conductivity. *Adv. Mater.* **29**, 1700339 (2017).
33. Y. Pan, Y. Guo, J. Liu, H. Zhu, G. Chen, Q. Liu, G. Liu, W. Jin, PDMS with tunable side group mobility and its highly permeable membrane for removal of aromatic compounds. *Angew. Chem. Int. Ed.* **61**, e202111810 (2022).
34. M.-J. Tang, M.-L. Liu, D.-A. Wang, D.-D. Shao, H.-J. Wang, Z. Cui, X.-L. Cao, S.-P. Sun, Precisely patterned nanostrand surface of cucurbituril[*n*]-based nanofiltration membranes for effective alcohol–water condensation. *Nano Lett.* **20**, 2717–2723 (2020).
35. H. Zhang, K. Wang, J. Li, J. Li, R. Zhang, Y. Zheng, Liquid-based nanogenerator fabricated by a self-assembled fluoroalkyl monolayer with high charge density for energy harvesting. *Matter* **5**, 1466–1480 (2022).
36. J. Wei, J. Zhang, X. Cao, J. Huo, X. Huang, J. Zhang, Durable superhydrophobic coatings for prevention of rain attenuation of 5G/weather radomes. *Nat. Commun.* **14**, 2862 (2023).
37. T. Zhou, R. T. Anderson, H. Li, J. Bell, Y. Yang, B. P. Gorman, S. Pylypenko, M. T. Lusk, A. Sellinger, Bandgap tuning of silicon quantum dots by surface functionalization with conjugated organic groups. *Nano Lett.* **15**, 3657–3663 (2015).
38. M. Jin, H. Lee, C. Im, H. J. Na, J. H. Lee, W. H. Lee, J. Han, E. Lee, J. Park, Y. S. Kim, Interfacial ion-trapping electrolyte-gated transistors for high-fidelity neuromorphic computing. *Adv. Funct. Mater.* **32**, 2201048 (2022).
39. O. Tricinci, F. Pignatelli, V. Mattoli, 3D micropatterned functional surface inspired by *Salvinia molesta* via direct laser lithography for air retention and drag reduction. *Adv. Funct. Mater.* **33**, 2206946 (2023).
40. X. Zhang, M. Scaraggi, Y. Zheng, X. Li, Y. Wu, D. Wang, D. Dini, F. Zhou, Quantifying wetting dynamics with triboelectrification. *Adv. Sci.* **9**, 2200822 (2022).
41. L. Chen, G. Shi, J. Shen, B. Peng, B. Zhang, Y. Wang, F. Bian, J. Wang, D. Li, Z. Qian, G. Xu, G. Liu, J. Zeng, L. Zhang, Y. Yang, G. Zhou, M. Wu, W. Jin, J. Li, H. Fang, Ion sieving in graphene oxide membranes via cationic control of interlayer spacing. *Nature* **550**, 380–383 (2017).
42. J. Lee, T. Laoui, R. Karnik, Nanofluidic transport governed by the liquid/vapour interface. *Nat. Nanotechnol.* **9**, 317–323 (2014).
43. S. Santoro, A. H. Avci, A. Politano, E. Curcio, The advent of thermoplasmonic membrane distillation. *Chem. Soc. Rev.* **51**, 6087–6125 (2022).
44. Z. Hu, F. Chu, H. Shan, X. Wu, Z. Dong, R. Wang, Understanding and utilizing droplet impact on superhydrophobic surfaces: Phenomena, mechanisms, regulations, applications, and beyond. *Adv. Mater.* **36**, e2310177 (2024).
45. Y. Chen, K.-J. Lu, S. Japip, T.-S. Chung, Can composite Janus membranes with an ultrathin dense hydrophilic layer resist wetting in membrane distillation? *Environ. Sci. Technol.* **54**, 12713–12722 (2020).
46. R. Zangi, J. B. Engberts, Physisorption of hydroxide ions from aqueous solution to a hydrophobic surface. *J. Am. Chem. Soc.* **127**, 2272–2276 (2005).
47. X. Zhang, H. Liu, L. Jiang, Wettability and applications of nanochannels. *Adv. Mater.* **31**, e1804508 (2019).
48. T. Kawasaki, K. Kim, Identifying time scales for violation/preservation of Stokes-Einstein relation in supercooled water. *Sci. Adv.* **3**, e1700399 (2017).
49. R. Duan, X. Lv, W. Yan, Y. Zhou, C. Gao, Fabrication of high boron removal reverse osmosis membrane with broad industrial application prospect by introducing sulfonate groups through a polyvinyl alcohol coating. *J. Membr. Sci.* **664**, 121079 (2022).
50. S. Asim, M. Wasim, A. Sabir, M. Shafiq, H. Andlib, S. Khuram, A. Ahmad, T. Jamil, The effect of nanocrystalline cellulose/Gum Arabic conjugates in crosslinked membrane for antibacterial, chlorine resistance and boron removal performance. *J. Hazard. Mater.* **343**, 68–77 (2018).
51. Y. Li, S. Wang, X. Song, Y. Zhou, H. Shen, X. Cao, P. Zhang, C. Gao, High boron removal polyamide reverse osmosis membranes by swelling induced embedding of a sulfonyl molecular plug. *J. Membr. Sci.* **597**, 117716 (2020).
52. Z. Ali, Y. Al Sunbul, F. Pacheco, W. Ogieglo, Y. Wang, G. Genduso, I. Pinnau, Defect-free highly selective polyamide thin-film composite membranes for desalination and boron removal. *J. Membr. Sci.* **578**, 85–94 (2019).
53. C. Li, Y. Zhao, G. S. Lai, R. Wang, Fabrication of fluorinated polyamide seawater reverse osmosis membrane with enhanced boron removal. *J. Membr. Sci.* **662**, 121009 (2022).
54. J. Hu, Y. Pu, M. Ueda, X. Zhang, L. Wang, Charge-aggregate induced (CAI) reverse osmosis membrane for seawater desalination and boron removal. *J. Membr. Sci.* **520**, 1–7 (2016).
55. S. Shultz, M. Bass, R. Semiat, V. Freger, Modification of polyamide membranes by hydrophobic molecular plugs for improved boron rejection. *J. Membr. Sci.* **546**, 165–172 (2018).
56. S. Wang, Y. Zhou, C. Gao, Novel high boron removal polyamide reverse osmosis membranes. *J. Membr. Sci.* **554**, 244–252 (2018).
57. R. Verbeke, V. Gomez, I. F. J. Vankelecom, Chlorine-resistance of reverse osmosis (RO) polyamide membranes. *Prog. Polym. Sci.* **72**, 1–15 (2017).
58. Y. Yao, P. Zhang, C. Jiang, R. M. DuChanois, X. Zhang, M. Elimelech, High performance polyester reverse osmosis desalination membrane with chlorine resistance. *Nat. Sustain.* **4**, 138–146 (2021).
59. Y. Hou, P. Shah, V. Constantoudis, E. Gogolides, M. Kappl, H.-J. Butt, A super liquid-repellent hierarchical porous membrane for enhanced membrane distillation. *Nat. Commun.* **14**, 6886 (2023).
60. Z. Sheng, J. Zhang, J. Liu, Y. Zhang, X. Chen, X. Hou, Liquid-based porous membranes. *Chem. Soc. Rev.* **49**, 7907–7928 (2020).
61. T. Tong, S. Zhao, C. Boo, S. M. Hashmi, M. Elimelech, Relating silica scaling in reverse osmosis to membrane surface properties. *Environ. Sci. Technol.* **51**, 4396–4406 (2017).
62. C. J. Van Oss, M. K. Chaudhury, R. J. Good, Interfacial Lifshitz-van der Waals and polar interactions in macroscopic systems. *Chem. Rev.* **88**, 927–941 (1988).
63. S. Gadipelli, W. Travis, W. Zhou, Z. Guo, A thermally derived and optimized structure from ZIF-8 with giant enhancement in CO_2 uptake. *Energ. Environ. Sci.* **7**, 2232–2238 (2014).
64. Y. Yusof, M. R. Johan, Concentration-dependent properties of amorphous carbon nanotube/silica composites via the sol–gel technique. *CrstEngComm* **16**, 8570–8575 (2014).
65. X. Yuan, J.-X. Wang, Y. Li, H. Huang, J. Wang, T. Shi, Y. Deng, Q. Yuan, R. He, P. K. Chu, X. F. Yu, Multilevel information encryption based on thermochromic perovskite microcapsules via orthogonal photic and thermal stimuli responses. *ACS Nano* **18**, 10874–10884 (2024).
66. D. Daniel, X. Yao, J. Aizenberg, Stable liquid jets bouncing off soft gels. *Phys. Rev. Lett.* **120**, 028006 (2018).
67. A. Deshmukh, C. Boo, V. Karanikola, S. Lin, A. P. Straub, T. Tong, D. M. Warsinger, M. Elimelech, Membrane distillation at the water-energy nexus: Limits, opportunities, and challenges. *Energ. Environ. Sci.* **11**, 1177–1196 (2018).
68. C. Liu, W. Wang, B. Yang, K. Xiao, H. Zhao, Separation, anti-fouling, and chlorine resistance of the polyamide reverse osmosis membrane: From mechanisms to mitigation strategies. *Water Res.* **195**, 116976 (2021).
69. M. Förster, M. Bohnet, Influence of the interfacial free energy crystal/heat transfer surface on the induction period during fouling. *Int. J. Therm. Sci.* **38**, 944–954 (1999).
70. A. Hina, G. Nancollas, M. Grynpas, Surface induced constant composition crystal growth kinetics studies. The brushite–gypsum system. *J. Cryst. Growth* **223**, 213–224 (2001).

Acknowledgments: We acknowledge the technical support from the Advanced Instrumental Analysis Center, School of Chemical Engineering and Technology, Tianjin University, for their provision of high-performance characterization services. We would like to thank Shiyanjia Lab (www.shiyanjia.com) for the analysis. **Funding:** S.Z. acknowledges funding from the National Natural Science Foundation of China (no. 22278304) and the exploratory project from the

State Key Laboratory of Chemical Engineering (no. SKL-ChE-23T07). **Author contributions:** L.Z. and S.Z. designed the research and wrote the initial draft. L.Z. performed the experiment including membrane fabrication, characterization, and performance test. T.Y. performed the molecular dynamic simulations. Z.Z. and Z.W. provided constructive suggestions for data visualization. S.L. and S.Z. contributed to revising the manuscript and provided constructive suggestions for the results. All authors discussed the results. **Competing interests:** The authors declare that they have no competing interests. **Data and materials availability:** All data needed to evaluate the conclusions in the paper are present in the paper and/or the Supplementary Materials.

Submitted 17 November 2024
Accepted 7 April 2025
Published 9 May 2025
10.1126/sciadv.adu6787